J Mater Sci
DOI 10.1007/s10853-015-9301-9

50TH ANNIVERSARY

Low-voltage ferroelectric–paraelectric superlattices as gate materials for field-effect transistors

I. B. Misirlioglu[1] · C. Sen[1] · M. T. Kesim[2] · S. P. Alpay[2,3]

Received: 23 July 2015 / Accepted: 24 July 2015

Abstract The demand for new materials to be used in field-effect transistors and similar devices with low energy loss is more than ever before as integrated circuits have become a considerable source of energy consumption. One of the challenges in designing such energy efficient logic devices is finding suitable dielectric materials systems for the gate that controls the drain current in a *p*-type channel. A fundamental limit for energy efficiency exists in such devices imposed by the polarizability of conventional linear gate dielectrics. Generating on/off states in the channel that differ by at least a million times in the magnitude of the drain current near saturation requires several volts of gate bias for the case of a linear dielectric material in a submicron device. In this study, we demonstrate that ferroelectric–paraelectric superlattice heterostructures can generate the same effect in a *p*-type channel for bias voltages much lower than in a linear high dielectric constant gate. We consider a metal/superlattice/*p*-type semiconductor stack for this purpose. Using a thermodynamic model, we show that the multi-domain state of the ferroelectric layers can be tailored and distinct on/off states of the channel are possible for gate bias voltages below 1 V. The origins of such functionality of ferroelectric–paraelectric superlattices are discussed with respect to material characteristics such as the phase transition temperature of the ferroelectric, total polarization, and the dielectric response.

✉ S. P. Alpay
pamir.alpay@uconn.edu

[1] Faculty of Engineering and Natural Sciences, Sabanci University, Tuzla/Orhanli, 34956 Istanbul, Turkey

[2] Department of Materials Science and Engineering and Institute of Materials Science, University of Connecticut, Storrs, CT 06269, USA

[3] Department of Physics, University of Connecticut, Storrs, CT 06269, USA

Introduction

Integration of materials with unusual properties into electronic devices paves the way for further developments and new functionalities. Such a trend has certainly been taking place in logic devices [1–5] such as the field-effect and metal–oxide–semiconductor transistors (FET and MOSFET, respectively), where control of current in a semiconductor (SC) channel through a gate is the main principle of operation. In particular, ever shrinking device dimensions have led to the search for new materials and multilayer heterostructures that enable faster operation, lower leakage currents between the gate and the channel. Moreover, the recent demand for low power consumption presents an additional challenge in designing such devices.

Use of ferroelectric (FE) oxides as gate materials to induce on/off states in the channel of a FET type device has attracted significant interest since FEs possess a switchable remnant polarization. Switching the polarization direction via the gate bias can induce on/off states in the channel corresponding to significant differences in carrier densities between the two states, an outcome desired in a binary logic device not operating at ultra-high frequencies. Another motivation behind exploring FE-gated FETs [4–13] is that the electric field switchable remnant polarization could potentially be used as an additional functionality to store data, thus enabling, for example, a non-volatile gate memory. While FEs are certainly viable candidates to replace linear dielectrics in such devices, the sensitivity of functional properties of FEs to residual strains, interfaces,

Published online: 05 August 2015

defects and electrostatic boundary conditions (BCs) are well known and must be taken into account [14–26]. For FE systems to become alternatives to current materials employed in FET/MOSFET, materials properties from a FE layer need to be comparable, if not better, than what is presently employed in device applications.

The polarization response, the dielectric constant, and electromechanical properties of FE are strongly temperature dependent. Regardless whether the paraelectric (PE)–FE phase transformation is first- or second-order, there is an anomaly in the property coefficients near the PE–FE transformation at the Curie temperature T_C. The FE is more polarizable (or permeable and "soft") when T_C is close to the operating (ambient) temperature compared to being "harder" if the ambient temperature is much lower than T_C. High dielectric constants are thus possible in the vicinity of T_C, leading to efforts to target this temperature regime to enhance second-order property coefficients for a wide spectrum of applications. T_C of a FE oxide can be adjusted via controlling the strain state of the structure (for instance, by means of the choice of the substrate) [27–30] or judicious doping/alloying of the FE [31, 32].

Another unique way to control T_C is by growing alternating layers of FE and PE materials [33, 34]. These superlattices typically consist of ultra-thin repeating units of FEs and PEs, usually not exceeding 20 nm per layer. The idea is that stacking FEs with PEs or linear dielectrics might generate interface-driven interactions. Very high dielectric responses from such structures have already been reported [35–43]. In addition, there are other unexpected properties [16, 44–50] such as the demonstration of the formation of interfacial layers that behave different than the "bulk" (midsection) of the layers with reduced tetragonality [46], appearance of ferroelectricity in paraelectric layers due to internal strain and electrical fields [51, 52], and the disappearance of the dielectric anomaly at the FE transition [69]. It is now well understood that it is the periodic contact between FE and PE layers that generates internal electric fields opposing the FE polarization, and therefore, reducing the T_C of the structure with respect to the ideal metal/FE/metal case. That the FE layer tries to cope with the internal fields via formation of electrical domains is another phenomenon behind various interesting observations and predictions on these systems [46, 53–55].

Overall, the presence of a potentially very high dielectric response from a FE/PE superlattice stack and that this response can be controlled with small bias values (<1 V) opens up the possibility to employ these structures as the gate in FET type devices. We note that such interface driven phenomena have resulted in significant developments in magnetic multilayers and paved the way for new generation of devices based on the giant magneto-resistance in ferromagnetic/metal/ferromagnetic hetero-layers [56]. In this study, we analyze the characteristics and properties of a FE/PE superlattice-semiconductor interface and mechanisms by which a FE/PE superlattice stack can alter carrier distribution in a *p*-type semiconductor (pSC) similar to that of a channel in a FET or MOSFET. We use non-linear thermodynamics based on Landau–Ginzburg–Devonshire (LGD) theory and couple this with relevant Maxwell equations for dielectric solids to compute the polarization in the superlattice. By combining these results with Fermi–Dirac distribution of charged carriers and ionized dopants in the superlattice and SC, we show that effective carrier control can be achieved with gate bias values much lower than those for an ordinary linear dielectric material. The multi-domain (MD) state of the FE/PE structure that may form due to depolarizing fields in the FE layers is the key to form a discontinuous or a continuous carrier gas at the superlattice/pSC interface leading to insulating-to-conducting transitions of the channel. The system that we investigate in detail in this study is a $PbZr_{0.3}Ti_{0.7}O_3$/$SrTiO_3$·(PZT/STO)·FE/PE superlattice heterostructure sandwiched between pSC and Pt electrodes. PZT/STO is specifically chosen because of the relatively low misfit between PZT and STO (~1 % at room temperature, RT). We calculate electrical domain configurations based on the number of repeating PZT–STO units and provide numerical results of the overall polarization as a function of temperature and the charge concentration variation with gate voltage. Our results demonstrate clearly that such multilayer heterostructures have indeed the potential to be employed as gate oxides in FETs and/or MOSFETs.

Theoretical approach

A schematic drawing of the PZT/STO superlattice system considered in our model is given in Fig. 1. We specifically study equi-thickness PZT/STO systems although such a restriction can be relatively easily relaxed [57]. As defined in Fig. 1, λ is the thickness of the repeating unit, n is the number of repeating units, d is the thickness of the metal and the SC layer, and L is the total thickness of the superlattice. The stacks are taken as being infinite along the *y*-direction, reducing the problem to two dimensions. We assume that all layers are grown pseudomorphically onto a (001) STO substrate and the system is short-circuited. The SC bottom electrode, namely the channel, is heavily *p*-doped with shallow acceptor dopants at a concentration of 10^{24} m^{-3} with each acceptor atom receiving one electron from the valence band and is grounded at all times, while the superlattice constituents are considered to be intrinsic wide band gap layers. The semiconducting parameters of the pSC, FE, and PE layers are provided in Table 1 [32, 58–60].

Maxwell equations as applied to the FE/PE superlattice and the pSC layer are satisfied such that:

$$\nabla \cdot \mathrm{D} = \rho \tag{1}$$

and we can express dielectric displacement vector as:

$$\mathrm{D} = (D_x, 0, D_z) \tag{2}$$

where

$$D_x = \varepsilon_o \varepsilon_b E_x + P_x \text{ and } D_z = \varepsilon_o \varepsilon_b E_z + P_z \tag{3}$$

in the FE/PE with x and z denoting the in-plane and out-of-plane components respectively and,

$$D_x = \varepsilon_0 \varepsilon_r E_x \text{ and } D_z = \varepsilon_0 \varepsilon_r E_z \tag{4}$$

in the pSC that has a dielectric constant of ε_r. The top metal is assumed to behave as an ideal metal and no electric field can penetrate it (meaning the screening length is unphysically thin) but its potential can be controlled externally. In Eqs. 3 and 4, ε_o is the permittivity of vacuum and ε_b is the background dielectric constant (taken as seven here [61, 62]) of the FE/PE (same value in both layers), E_x and E_z are components of the electric field vector $\mathbf{E} = (E_x, 0, E_z)$ which follow from $E_x = -\partial\phi/\partial x$ and $E_z = -\partial\phi/\partial z$ and, and P_x and P_z are the components of the polarization vector $\mathbf{P} = (P_x, 0, P_z)$. ρ is the total charge density and consists of electrons and holes in the FE/PE, pSC in addition to ionized acceptors that are present only in the pSC channel:

$$\rho = q(-n^- + p^+ - N_A^-) \tag{5}$$

where

$$N_A^- = N_A \left(\exp\left(\frac{q(E_A - E_F - \phi)}{kT} \right) + 1 \right)^{-1} \tag{6a}$$

$$n^- = N_C \left(\exp\left(\frac{q(E_C - E_F - \phi)}{kT} \right) + 1 \right)^{-1} \tag{6b}$$

$$p^+ = N_V \left[1 - \left(\exp\left(\frac{q(E_V - E_F - \phi)}{kT} \right) + 1 \right)^{-1} \right] \tag{6c}$$

N_A^- is the ionized acceptor density in the pSC, n^- is the electron density at any given coordinate except the top metal electrode, p^+ is the hole density, N_C is the effective density of states at the bottom of the conduction band and N_V is the effective density of states at the top of the valence band of a given layer (except the top metal), E_C is the energy of an electron at the bottom of the conduction band, E_V is the energy of an electron at the top of the valence band, E_F is the Fermi level, ϕ is the local electrostatic potential and E_A is the ionization energy of the acceptor atom that is taken with respect to the top of the valence band, k is the Boltzmann constant in eV units, and T is temperature in Kelvin. To carry out the calculations including the band bending in the FE/PE stack, one needs to know E_F of the metal/FE/PE/pSC structure which is taken to be that of Pt as the stack will equilibrate with the Fermi level of Pt upon contact.

The electrostatic BCs for the potential are needed to obtain solutions to the Eqs. 1–6. The BCs for the electrostatic potential along the thickness of the superlattice is:

$$\phi_{FE} = \phi_{pSC} \text{ for } z = n\lambda/2, \tag{7}$$

where n is an integer denoting a PE/FE interface and Eq. 7 ensures the continuity of the potential at each interface and

$$\phi_{metal} = \phi_{pSC} = 0 \text{ for } z = 0, L \tag{8}$$

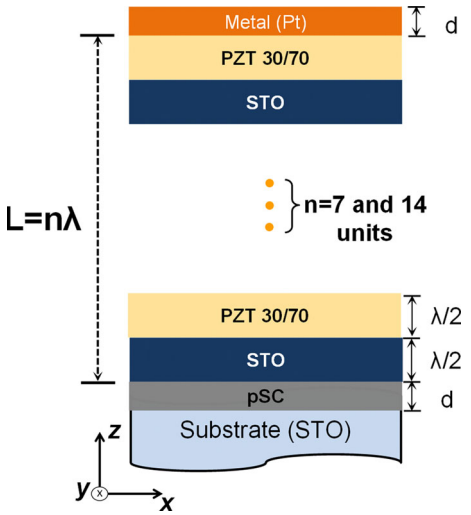

Fig. 1 A schematic drawing of the superlattice for which the computations are carried out. λ and d are the thickness of the repeating unit and Pt or pSC, respectively. n is the number of repeating units and L is the total thickness of the metal/FE/PE/pSC heterostructure on STO (Color figure online)

Table 1 Band parameters, ionization energies of dopants and linear dielectric values the pSC, nSC, and the FE used in the calculations

	E_F (eV)	N_C (m^{-3} E^{-1})	N_V (m^{-3} E^{-1})	N_A (m^{-3})	E_A, E_D (eV)	E_C, E_V (eV)	ε_r (ε_b in FE)
pSC	−5.1	10^{25}	10^{25}	10^{24}	−0.05	−4.05, −5.15	10
FE	−5.7	10^{24}	10^{24}	none	none	−4.2, −7.4	7
PE	−5.4	10^{24}	10^{24}	none	none	−3.9, 7.1	7

m^{-3} E^{-1} is the unit for density of states (E energy unit, eV)

for short circuiting conditions where we assumed the Pt top metal electrode behaves ideal (the electric field does not penetrate into the electrode) and the bottom Pt electrode contacting the pSC is ideal as well. When a bias is applied to the system, potential in the top metal is raised or lowered depending on the sign of the bias with respect to the other end of the stack, i.e., the bottom electrode, which is electrically grounded at all times. Note that, before considering any external bias effects, the condition of equality of electrochemical potential causing charge transfer between the layers automatically imposes the presence of a built-in field in the FE/PE superlattice and a position-dependent depletion charge distribution as a consequence. The electric field in the FE/PE superlattice satisfies the LGD equations of state given as:

$$\begin{aligned} & w\Big\langle 2\alpha_3^m P_z + 4\alpha_{13}^m P_z P_x^2 + 4\alpha_{33}^m P_z^3 + 6\alpha_{111} P_z^5 \\ & \quad + \alpha_{112}(4P_z P_x^4 + 8P_z^3 P_x^2) + 2\alpha_{123} P_z P_x^4 - \gamma\left(\frac{\partial^2 P_z}{\partial z^2} + \frac{\partial^2 P_z}{\partial x^2}\right)\Big\rangle_{\mathrm{FE}} \\ & + (1-w)\Big\langle 2\alpha_3^m P_z + 4\alpha_{13}^m P_z P_x^2 + 4\alpha_{33}^m P_z^3 - \gamma\left(\frac{\partial^2 P_z}{\partial z^2} + \frac{\partial^2 P_z}{\partial x^2}\right)\Big\rangle_{\mathrm{PE}} \\ & = wE_z + (1-w)E_z \end{aligned} \tag{9a}$$

$$\begin{aligned} & 2\alpha_1^m P_x + 2(2\alpha_{11}^m + \alpha_{12}^m)P_x^3 + 2\alpha_{13}^m P_x P_z^2 + 6\alpha_{111} P_x^5 + \\ & w\Big\langle 2\alpha_{112}[3P_x^5 + 3P_x^3 P_z^2 + P_x P_z^4] + 2\alpha_{123} P_x^3 P_z^2 - \gamma\left(\frac{\partial^2 P_x}{\partial z^2} + \frac{\partial^2 P_x}{\partial x^2}\right)\Big\rangle_{\mathrm{FE}} \\ & + (1-w)\Big\langle 2\alpha_1^m P_x + 2(2\alpha_{11}^m + \alpha_{12}^m)P_x^3 + 2\alpha_{13}^m P_x P_z^2 - \gamma\left(\frac{\partial^2 P_x}{\partial z^2} + \frac{\partial^2 P_x}{\partial x^2}\right)\Big\rangle_{\mathrm{PE}} \\ & = wE_x + (1-w)E_x \end{aligned} \tag{9b}$$

Here, w is an arbitrary function we introduce to assign the coordinates of the FE/PE interfaces and the repeating unit thickness of the superlattice (λ) and determine the total superlattice thickness. w is valid only in the superlattice as defined below:

$$\Omega = \mathrm{sgn}(\sin\frac{2\pi z}{\lambda}), \tag{10}$$

where z is thickness from the bottom pSC/superlattice interface to the top superlattice/metal interface (Fig. 1). Using the values of Ω we choose:

$$\text{FE layer } \rightarrow \text{ if } \Omega > 0, \text{ PE layer } \rightarrow \text{ if } \Omega < 0, \tag{11a}$$

and therefore

$$w = 1 \text{ if } \Omega > 0 \text{ and } w = 0 \text{ otherwise.} \tag{11b}$$

In Eqs. 9a and 9b; α_1^m, α_3^m α_{11}^m, α_{33}^m,α_{12}^m, and α_{13}^m are the renormalized dielectric stiffness coefficients in SI units given by:

$$\alpha_1^m = \alpha_1 - u_m\frac{2(Q_{11}+Q_{12})}{s_{11}+s_{12}},\ \alpha_3^m = \alpha_1 - u_m\frac{4Q_{12}}{s_{11}+s_{12}}, \tag{12a}$$

$$\begin{aligned} \alpha_{11}^m &= \alpha_{11} + \frac{2}{s_{11}^2 - s_{12}^2}\left[(Q_{11}^2+Q_{12}^2)s_{11} - 2Q_{11}Q_{12}s_{12}\right],\ \alpha_{33}^m \\ &= \alpha_{11} + \frac{4Q_{12}^2}{s_{11}+s_{12}}, \end{aligned} \tag{12b}$$

$$\begin{aligned} \alpha_{12}^m &= \alpha_{12} - \frac{2}{s_{11}^2 - s_{12}^2}\left[(Q_{11}^2+Q_{12}^2)s_{12} - 2Q_{11}Q_{12}s_{11}\right] \\ &\quad + \frac{Q_{44}^2}{s_{44}},\ \alpha_{13}^m \\ &= \alpha_{12} + \frac{2Q_{12}(Q_{11}+Q_{12})}{s_{11}+s_{12}}, \end{aligned} \tag{12c}$$

where $\alpha = (2\varepsilon_0 C)^{-1}$, Q_{ij} and S_{ij} are electrostrictive coefficients and components of the elastic stiffnesses at constant polarization, respectively, and α_i, α_{ij}, and α_{ijk} are the dielectric stiffness coefficients of bulk PZT. We note that α_{12}^m and α_{33}^m contain the clamping effect of the film, γ is the gradient energy coefficient and is assumed to be isotropic for convenience and is taken to be 6×10^{-10} m^3 F^{-1} [63]. The thermodynamic, elastic, and electromechanical data used in the calculations are given in Table 2 [32, 59, 60].

The pseudo-cubic (polarization-free) misfit strain tensor in PZT is defined as:

Table 2 Bulk thermodynamic, elastic, and electromechanical coefficients of PZT 30/70 and STO

	PZT 30/70	STO
a (nm)	0.3950	0.3904
T_C (°C)	440.2	−253
C (10^5 °C)	1.881	0.8
Q_{11}(m^4 C^{-2})	0.07887	0.0457
Q_{12}(m^4 C^{-2})	−0.02480	−0.013
Q_{44}(m^4 C^{-2})	0.06356	0.00957
s_{11}(10^{-12} N m^{-2})	8.4	3.729
s_{12}(10^{-12} N m^{-2})	−2.7	−0.9088
s_{44}(10^{-12} N m^{-2})	17.5	
α_{11}(10^7 N m^6 C^{-4})	0.6458	170
α_{12} (10^8 N m^6 C^{-4})	5.109	27.4
α_{111} (10^8 N m^{10} C^{-6})	2.348	–
α_{112} (10^8 N m^{10} C^{-6})	10.25	–
α_{123} (10^9 N m^{10} C^{-6})	−5.003	–
γ (10^{-10} N m^4 C^{-2})	6	6

$$u_{ij}^{m} = \begin{pmatrix} u_{\mathrm{m}} & 0 & 0 \\ 0 & u_{\mathrm{m}} & 0 \\ 0 & 0 & -2u_{\mathrm{m}}S_{12}/(S_{12}+S_{11}) \end{pmatrix} \text{ with } u_{\mathrm{m}} = \frac{a_{\mathrm{STO}} - a_{\mathrm{PZT}}}{a_{\mathrm{STO}}} \tag{13}$$

where u_{m} is the in-plane misfit strain which enters Eqs. 9a, 9b, and 12a, a_{STO} is the lattice parameter of the STO substrate (Fig. 1) and a_{PZT} is the pseudo-cubic bulk lattice parameter of PZT. Since all layers are assumed to be pseudomorphic, the in-plane misfit u_{m} in STO layers in the superlattice equals 0. The polarization-free misfit strain u_{m} in PZT is $\sim$3 % at RT which corresponds to an actual misfit of $\sim$1 % which ensures that the FE polarization is along the z-axis.

Periodic BCs are employed along the plane of the structures for polarization and the electrostatic potential as well. The polarization BCs at the FE/PE and metal/FE interfaces can be expressed as:

$$\left[P_z + \beta \frac{\mathrm{d}P_z}{\mathrm{d}z}\right]_{z=0,L} = 0, \tag{14a}$$

$$\left[P_x + \beta \frac{\mathrm{d}P_x}{\mathrm{d}z}\right]_{z=0,L} = 0 \tag{14b}$$

with z indicating the coordinates for metal/FE (top) and PE/pSC (bottom, $L = 0$) interfaces, β is the extrapolation length describing the extent of change of P_z (P_x) along (perpendicular to) the film normal at the interface and is a parameter describing how strongly ferroelectricity is suppressed near the electrode interfaces (taken as 3 nm here based on previous reports [61, 62]. We assume that the interfaces of the FE and PE layers are "neutral" with respect to the transition temperature of the interior of the layers. This means that the surfaces of the FE and PE layers are assumed to have the same T_{C} as bulk of the layers ($\beta \to \infty$). We do so to focus on the electrode interfaces as small values of β can complicate the analysis of the results. Furthermore, such an approach has yielded theoretical results [64] in very good agreement with experimental findings [65].

We employ a finite difference discretization in two dimensions and carry out a Gauss–Seidel iterative scheme to solve the coupled Eqs. 1, 4, 5, 11, and 14 simultaneously subject to the BCs provided in Eqs. 11–14. The computation grid consists of $m \times 200$ points where m is the number of nodes along the thickness that vary depending on the superlattice size considered (298 nodes for both the pSC and the superlattice and 1 node for top/bottom metal to specify the potential BCs, making a total of 300 nodes). The node-to-node distances, namely h, are taken as 0.4 nm, almost the unit cell size of the pseudo-cubic PZT and STO and, therefore, $mh = n\lambda$. We terminate the iteration after 3000 loops that yield a difference of less than 10^{-3} C m^{-2} for polarization between two consecutive steps. To ensure the correctness of the numerical solutions, we applied our approach to test cases such as homogeneous FE ($\beta \to \infty$) with ideal electrodes and FE sandwiched between 2 PE layers as in [64, 66] where we obtained excellent agreement with analytical solutions (not shown here).

Domain structures and transition temperatures of superlattices

We first focus on the effect of layer periodicity of the FE/PE superlattices as this determines the FE/PE transition temperature and potentially the bias enabling carrier density control. Anticipating that the carrier density at the superlattice/pSC interface will be a function of domain states and the magnitude of the (total) polarization, we start off with the domain structures of two stacks having the same total thickness of 105 nm but differing in number of units, namely $n = 7$ and 14 with repeating unit thicknesses $\lambda = 15$ and 7.5 nm, respectively. Polarization maps at RT are provided in Fig. 2. Each stack has the FE PZT layer as the first layer in contact with the top metal electrode and the structures both terminate with the PE STO layer. We chose to terminate the stacks with STO as this material provides a good barrier to leakage currents [67, 68] and has exceptional polarizability that would potentially allow the transmission of domain wall-related phenomena in the FE layer to the pSC interface. We have also analyzed two different thicknesses for each stack type as we would like to reveal the field dependence of the carrier density response at the superlattice/pSC interface. This, however, did not result in discernible differences in the results for the "take-off" bias, which is around 0.5 V, as shown in Fig. 3. This is because the transition temperature and thus the domain structure of the superlattice do not depend on the total thickness of the heterostructure but rather on the repeating unit thickness [66]. We note that the "take-off" bias might not necessarily correspond to onset of conduction in the p-type channel as the discrete carrier concentrations need to merge to form a continuous carrier sheet at the FE/pSC interface for the "on" state as we shall show in the next section. All what is discussed until here will certainly not be the case if the bias is much larger than what is used here to demonstrate channel control. Such high fields and their effects are outside the scope of the present study.

As such, we decided to focus on the domain states and transition characteristics of the relatively thick (105 nm) stacks. The 7-unit superlattice with metal top and bottom pSC electrodes is in a distinct MD state, while the 14-unit superlattice is either in a weak single domain (SD) or a very wide domain periodicity MD regime, i.e., the domain

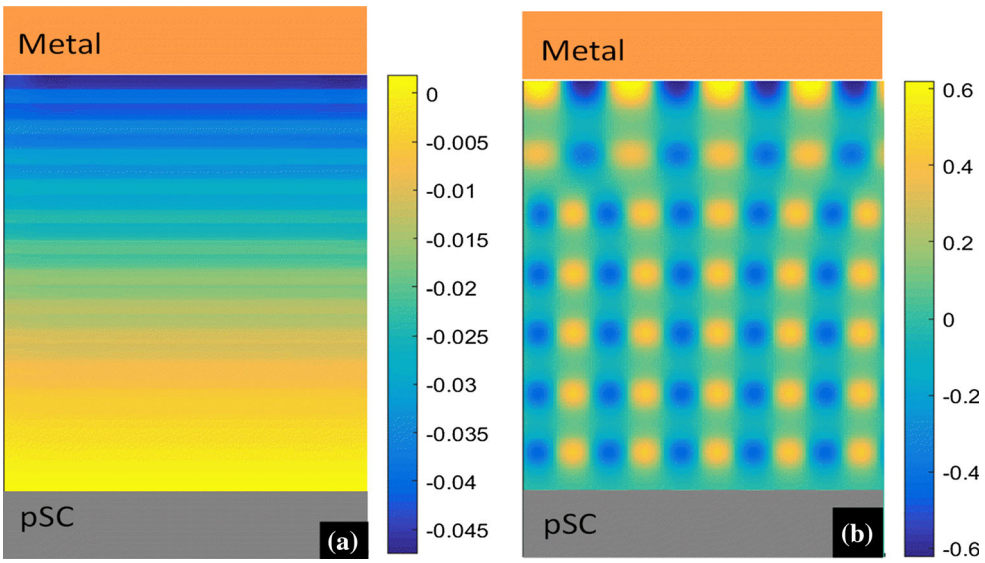

Fig. 2 RT out-of-plane polarization maps for 105-nm-thick PZT/STO superlattices with **a** $n = 14$ and **b** $n = 7$ repeating units on STO. The units on the vertical scales are in C/m^2. The polarization in the superlattice with $n = 14$ is considerably smaller than that of the superlattice with $n = 7$ due to relatively larger depolarizing fields

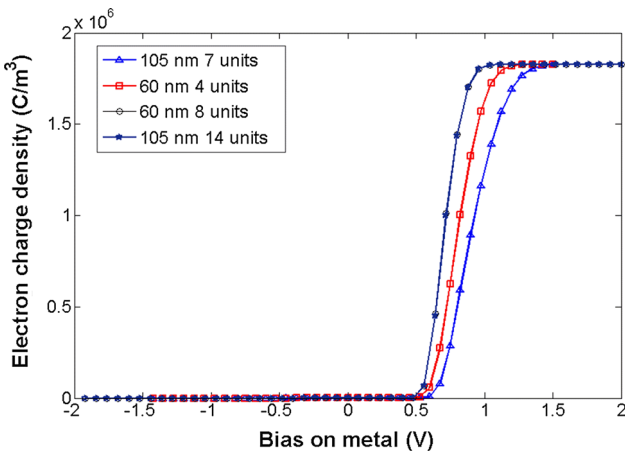

Fig. 3 Bias-dependent carrier density of PZT/STO superlattices as a function of n and L. The carrier density of the 60 nm stack with $n = 8$ is identical to that of 105-nm stack with $n = 14$ (Color figure online)

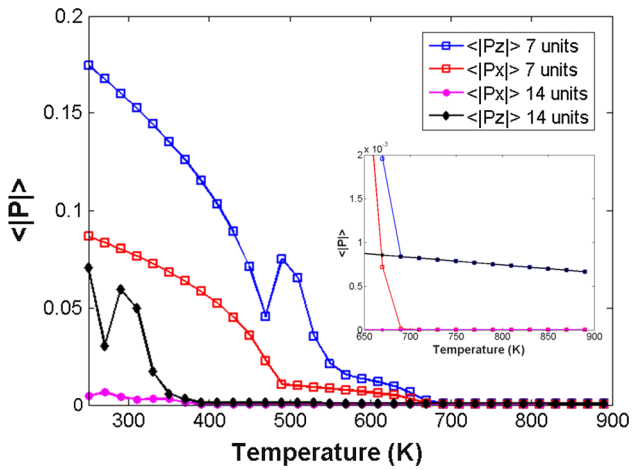

Fig. 4 Temperature-dependent absolute average values of in-plane $<|P_x|>$ and out-of-plane polarizations $<|P_z|>$ for 105-nm-thick PZT/STO superlattices with $n = 7$ and $n = 14$ repeating units on STO. The inset shows small built-in polarization due to the top/bottom electrode asymmetry. Note that the P_z for 14- and 7-unit stacks almost completely overlap and are hard to distinguish due to their identical dielectric response far above their respective T_C (Color figure online)

size is larger than the lateral grid size in the computations. It is almost certain that, in the light of prior experiments and theoretical predictions on such systems [64–66], the two stacks with different unit thicknesses will have different transition temperatures, which are computed and plotted as shown in Fig. 4. The transition temperatures of the two stacks can be found from investigating $<|P_z|>$ vs. temperature where the departing point of $<|P_z|>$ from the flat background polarization can be taken as the reference state. The stack with smaller n (14 units) has a FE transition temperature that is considerably lower than that of the stack with seven units. This also impacts the domain stabilities of the two stacks in comparison: the 7-unit stack is stabilized in the MD state while the 14-unit stack is apparently in a weak-SD state, where the latter is probably also favored by the asymmetry in top/bottom interfaces.

One should expect the stacks considered here to behave differently from those similar structures analyzed in previous studies since these have considered either ideal symmetrical top/bottom electrodes or infinite systems (periodic BCs) along the film/heterostructure thickness [64, 66, 69]. A small but finite built-in polarization due to the top–bottom electrode asymmetry is expected. This is indeed confirmed as shown in the inset of Fig. 4. In the case of symmetric top/bottom electrodes, no such built-in polarization exists as previously shown in detail in Ref. [69] and our results converge to that of shown in that paper.

Carrier density at the superlattice/pSC interface

The bias dependence of the carrier density near the superlattice/pSC interface is plotted in Fig. 5. We provide here the results for two stacks with different number of repeating units. Quite significant carrier density differences can be obtained at the superlattice/pSC interface within a small range of bias on the top metal. Carrier density maps for the 14 unit stack for two bias values of the top metal (0 and 0.8 V) are given in Fig. 6. There is about 11 orders of magnitude difference in the carrier density at the FE/pSC interface when stacks of 0 and 0.8 V are considered. This is in addition to the fact that 0 V bias results in "discrete" or "discontinuous" sheet-like carrier density compared to 0.8 V bias where there is a formation of a continuous film of carriers. Curves similar to what is provided in Fig. 5 for the positive gate voltages on the metal but for drain currents have been reported previously for other FE systems such as single layer $SrBi_2Ta_2O_9$ (SBT) [70]. Here, we are able to analyze the shape of such curves in the relatively simpler model systems in connection with the domain states and the transition temperatures.

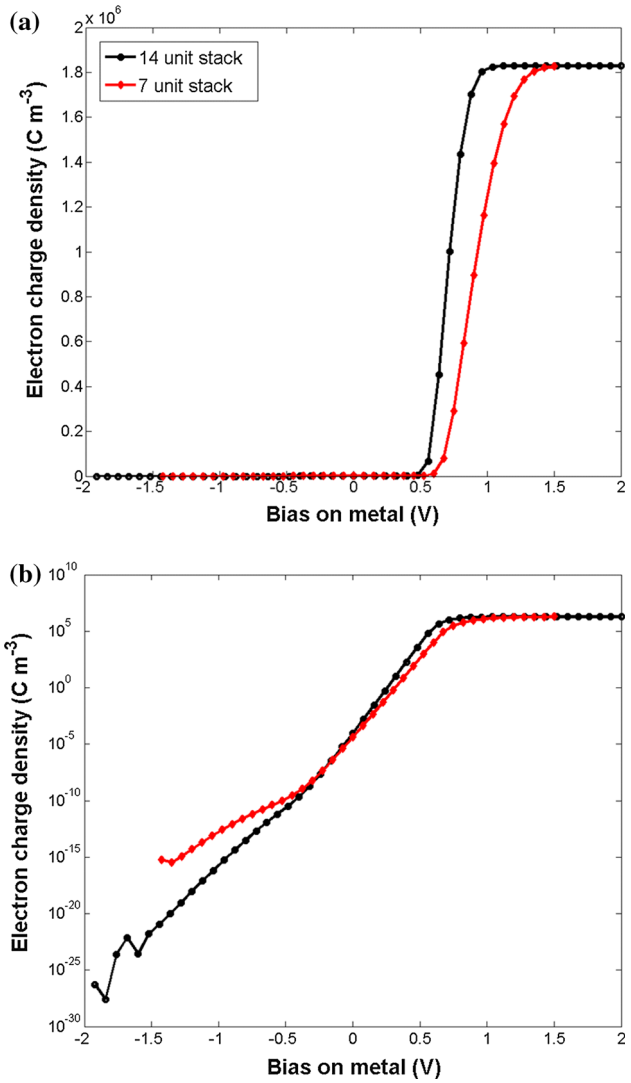

Fig. 5 Gate bias dependence of the electron charge density near the pSC/PZT interface for a 120-nm-thick pSC/PZT/STO heterostructure with $n = 7$ and 14 units. The same data are plotted on **a** linear and **b** logarithmic scales. The fluctuations of electron charge density at gate bias smaller than −1.25 V are due to the fact that numerical precision limit is reached by the computer and are not of physical origin (Color figure online)

An important outcome of our results is the relatively low bias values on the gate under which significant carrier densities can form on the pSC side of the superlattice/pSC interface. Particularly, the case of 14 units can reduce the necessary gate voltage to induce significant variations in pSC minority carrier densities, i.e., electrons, near the interface. Having stated that the polarization magnitude of the FE layers drives the accumulation of carriers, one also needs to consider the ease with which the domain walls move in response to an applied bias. The stack with the lower T_C should be expected to be "softer," i.e., should have relatively higher domain wall mobility, leading to a higher *effective* dielectric response.

It is clear from Eqs. 7, 8, 14 that polarization gradients determine the local electrostatic potential. As such, this is a non-linear problem, which makes it difficult to provide quantitative solutions. Nonetheless, we can attempt to analyze the amount of band bending near the FE/pSC interface and comment on the different extents of carrier accumulation near that interface in the two stacks to shed light on the effect of T_C and thus the polarization strength. In Figs. 7, 8, 9, we plot the flat-band energy diagrams that are calculated by imposing the electrostatic potential on the band energies of each materials system. We must point out that results will differ for domains with polarization along the positive and negative z-axis. Furthermore, electrical BCs such as the presence or absence of a bias voltage at the top electrode should affect the internal potential and, therefore, the flat-band diagram. The zero bias band bending, particularly in the seven unit stack, is reminiscent of multilayers/superlattices of polar semiconductors such as InN/GaN or GaN/AlN [71–73]. The difference here is that the bending is due to the presence of a FE polarization that is switchable (Fig. 7a) compared to the un-switchable ionic plus piezoelectric polarization in compound polar semiconductors. In the MD state, the bands in the positive and negative domains will have opposite slopes. Application of a positive bias to the top metal pulls down the potential values, the STO layer becomes polarized, minimizing the polarization mismatch at the interlayer interfaces. This causes the potential profile of the bands to flatten as shown in the 7-unit stack (Fig. 7b). The zero bias band profile is rather smooth in the 14 unit stack as the polarization in the layers is almost constant due to a SD-

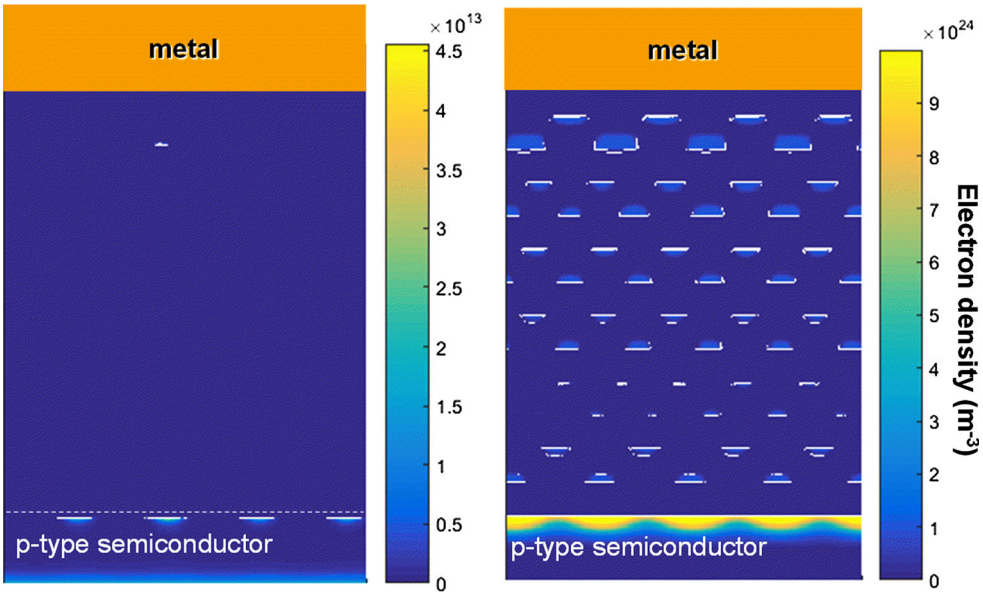

Fig. 6 RT carrier density map of 120-nm-thick pSC/PZT/STO heterostructure for **a** 0 V and **b** 0.8 V bias. For the stack with 0.8 V bias, the carrier density at the pSC/FE interface is more than 11 orders of magnitude higher than the stack with 0 V bias

like state (Fig. 8a) and a polarization with low but almost equal magnitude in the layers. A bias as small as 0.8 V can shift the entire band structure due to an almost constant polarization profile (please see Fig. 2a) owing to the high polarizability of the STO layers and that the stack is not far from T_C. A rather steep band bending, on the other hand, occurs on the pSC side as the superlattice polarization makes a jump whose bound charges can only be partially screened by the pSC (Fig. 8b). Apparently, a constant but small polarization termination near the superlattice/pSC interface has a stronger influence on the band bending in the pSC with respect to a MD state terminating at the same interface where the latter has an alternating sign of potential. Thus, the multilayer heterostructure with lower Curie temperature is more susceptible to becoming a SD state system, particularly in the presence of asymmetric top/bottom interfaces, favoring the behavior in Fig. 4. Keeping in mind that the slope of the band slope from the pSC side will determine the electron accumulation, we focus on the pSC/FE interfaces given in Fig. 8a, b. Indeed, Fig. 9 reveals that the amount of band bending in the pSC layer interfacing a 7-unit or a 14-unit stack is markedly different. The band diagram of the 14-unit superlattice has a relatively steeper slope and hence a higher accumulation of carriers. Such an occurrence originates from the softness of the polarization in the latter according to our results. Therefore, one can expect that a wide domain structure, or even a possibly weak-SD state near the transition temperature to generate significant carrier density differences in the pSC channel for on/off states owing to the susceptibility of polarization to applied bias. One can eventually expect that a SD state will lead to stronger band bending than an MD state where the latter has an electrostatic potential alternating in sign. Note that the temperature at which P_z changes its slope due to the appearance of P_x in the 14-unit stack is almost equal to RT. High dielectric response in this regime was shown previously [69]. However, due to the highly non-linear dependence of the dielectric constant on applied field in such structures and considering their high sensitivity to electrode interfaces, we realize such reasoning requires further detailed analysis that we leave to a future study. While a FET or MOSFET-type device can benefit from a FE/PE superlattice gate for channel control at relatively low bias values relative to linear ordinary dielectrics, a wide MD or a weak-SD state in the superlattice, occurring when the ambient operation temperature is not far from T_C, leads to a higher domain wall mobility under smaller fields and can allow more effective control of carrier densities in the pSC channel.

Summary and outlook

In this article, we theoretically analyzed the electrical properties and suitability of FE/PE superlattices when used as a gate material interfacing a *p*-type SC. We specifically study a PZT/STO FE/PE superlattice sandwiched between pSC and Pt electrodes. We calculate the electrical domain structure as a function of repeating PZT/STO units and provide numerical results of the overall polarization as a function of temperature and the charge concentration variation with gate voltage. Our results show that a MD state inevitably forms in superlattices consisting of relatively thick layers. This is in accordance with previous studies [39, 54, 64, 66, 74]. We also find that superlattices made up of relatively thinner layers may have a tendency

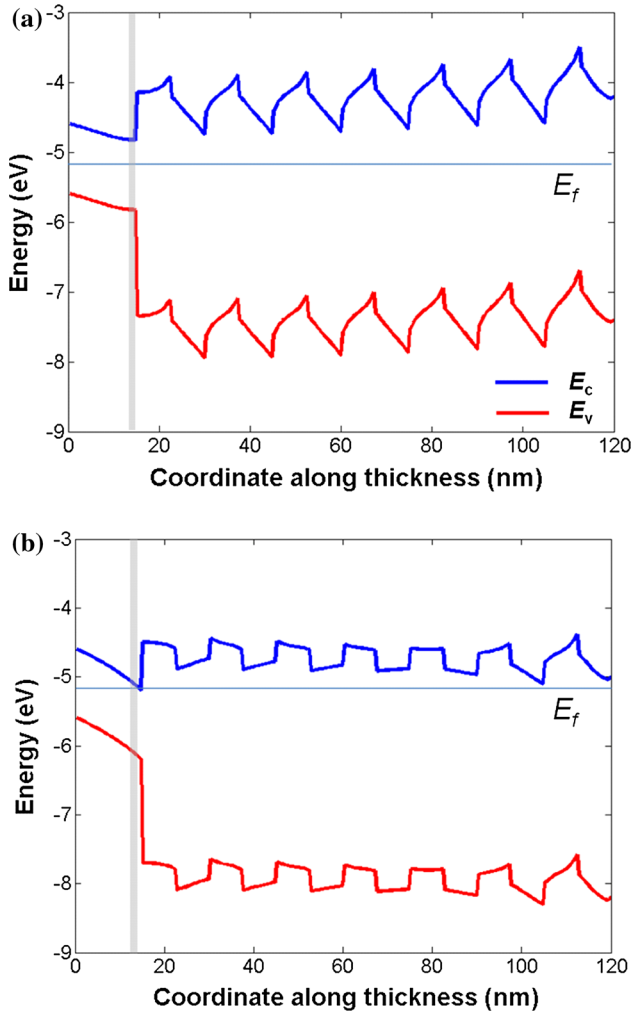

Fig. 7 Flat-band energy diagrams along z-direction for 120 nm-thick pSC/PZT/STO heterostructure under **a** zero and **b** 0.8 V bias on STO. The thickness of PZT/STO superlattice stack is 105 nm with $n = 7$ units. The highlighted region shows the pSC/superlattice interface that separates the pSC (*left side*) from the superlattice stack (*right side*) (Color figure online)

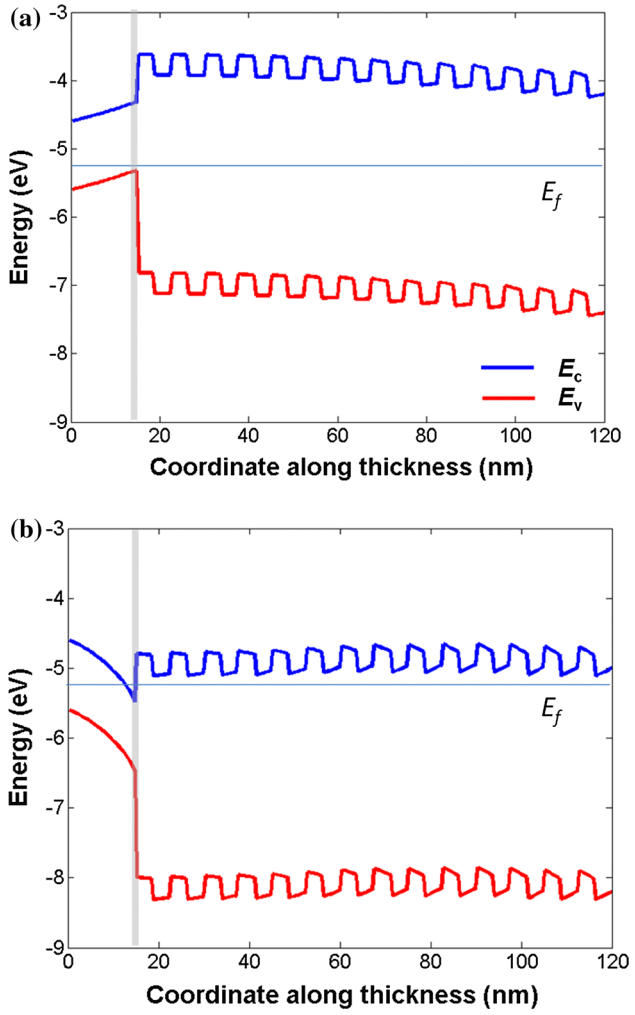

Fig. 8 Flat-band energy diagrams along z-direction for 120-nm-thick pSC/PZT/STO heterostructure with **a** zero and **b** 0.8 V bias on STO. The thickness of PZT/STO superlattice stack is 105 nm with $n = 14$ units. The highlighted region shows the pSC/superlattice interface that separates the pSC (*left side*) from the superlattice stack (*right side*) (Color figure online)

to exist in a MD state that consists of domains with a relatively large domain periodicity. These thinner superlattices may also be in a simple single-domain state but the formation of the monodomain state is accompanied by a reduction in the FE phase transformation temperature. Our calculations indicate that there is a significant difference between the electron density and the bias voltage for monodomain and MD superlattices. The stacks with thinner units display a more rapid bias-driven increase in electron density in the superlattice/pSC interface compared to the stacks with thicker repeating units. We explain this observation with the clearly different transition temperatures of the two stacks and different domain structures. The "softness" of the polarization in the stack with the lower transition temperature has a strong impact on the band bending. Our findings indicate that FE superlattices in the MD state can potentially be used as gates in FET/MOSFET-type architectures. The computations show that distinct on/off states of the SC channel are possible for gate bias voltages below 1 V.

We note that typically a high dielectric constant is required in the applications discussed herein—as gate materials enabling low power switching. However, in the off state, the gate itself should not store charge unless the gate is to act only as a switch and not a memory. Furthermore, D (or P)–E hysteresis is another phenomena that would generate losses and should be avoided as well, and the MD state that forms in superlattices actually provides the means to obtain non-hysteretic channel control. The materials systems we consider here could have a linear

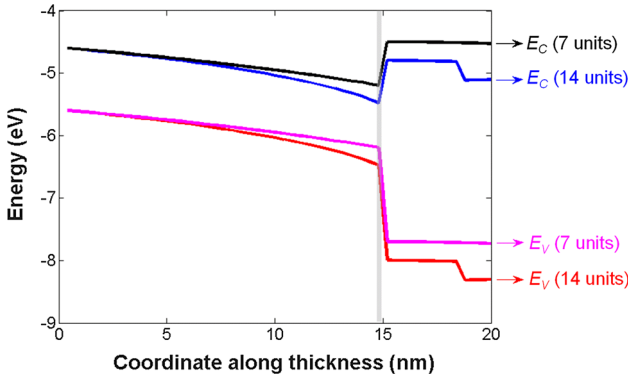

Fig. 9 Flat-band energy diagrams along z-direction (from 0 to 20 nm) for 120-nm-thick pSC/PZT/STO heterostructure with $n = 7$ and 14 units on STO at 0.8 V bias. The band banding near the pSC/superlattice interface (*highlighted region*) can clearly be seen for both heterostructures (Color figure online)

large effective dielectric response but we do not expect hysteretic losses associated with total polarization switching. Current leakage due to the presence of charged defects is another issue that factors into the device performance. The materials systems discussed here have excellent on/off switching properties and allow for additional functionalities such as a tunable dielectric constant. Taking into account the additional parameters that factor into device design such as dielectric loss and leakage, a materials genomics type of optimization [75] could be useful to explore the full potential of FE superlattices in FET/MOSFET type of applications.

Acknowledgements The authors gratefully acknowledge many discussions with Dr. J. V. Mantese (United Technologies Research Center, East Hartford, CT—USA). M. T. Kesim is supported by a GE Graduate Fellowship.

Compliance with ethical standards

Conflict of interest The authors declare that they have no conflict of interest.

References

1. Gruverman A, Wu D, Lu H, Wang Y, Jang HW, Folkman CM, Zhuravlev MY, Felker D, Rzchowki M, Eom CB, Tsymbal EY (2009) Tunneling electroresistance effect in ferroelectric tunnel junctions at the nanoscale. Nano Lett 9:3539–3543
2. Tsymbal EY, Gruverman A (2013) Ferroelectric tunnel junctions: beyond the barrier. Nat Mater 12:602–604
3. Lu H, Lipatov A, Ryu S, Kim DJ, Lee H, Zhuravlev MY, Eom CB, Tsymbal EY, Sinitski A, Gruverman A (2014) Ferroelectric tunnel junctions with graphene electrodes. Nature 5:1–7
4. Watanabe Y (1995) Epitaxial all-perovskite ferroelectric field effect transistor with a memory retention. Appl Phys Lett 66:1770–1772
5. Mathews S, Ramesh R, Venkatesan T, Benedetto J (1997) Ferroelectric field effect transistor based on epitaxial perovskite heterostructures. Science 276:238–240
6. Ma TP, Han J (2002) Why is nonvolatile ferroelectric memory field-effect transistor still elusive? IEEE Electron Device Lett 23:386–388
7. Hoffman J, Pan X, Reiner JW, Walker FJ, Han JP, Ahn CH, Ma TP (2010) Ferroelectric field effect transistors for memory applications. Adv Mater 22:2957–2961
8. Van Hai L, Takahashi M, Sakai S (2010) Fabrication and characterization of sub-0.6-μm ferroelectric-gate field-effect transistors. Semicond Sci Technol 25:115013
9. Salvatore GA, Lattanzio L, Bouvet D, Ionescu AM (2011) Modeling the temperature dependence of Fe-FET static characteristics based on Landau's theory. IEEE Trans Electron Devices 58:3162–3169
10. Salvatore GA, Lattanzio L, Bouvet D, Stolichnov I, Setter N, Ionescu AM (2010) Ferroelectric transistors with improved characteristics at high temperature. Appl Phys Lett 97:053503
11. Jiang B, Tang M, Li J, Xiao Y, Tang Z, Cai H, Lv X, Zhou Y (2012) Large memory window and good retention characteristics of ferroelectric-gate field-effect transistor with Pt/$Bi_{3.4}Ce_{0.6}Ti_3O_{12}$/$CeO_2$/Si structure. J Phys D 45:025102
12. Tanakamaru S, Hatanaka T, Yajima R, Takahaski M, Shigeki S, Takeuchi K (2009) A 0.5 V operation, 32 % lower active power, 42 % lower leakage current, ferroelectric 6T-SRAM with VTH self-adjusting function for 60 % larger static noise margin. In: IEEE international on electron devices meeting, IEDM, pp 283–286
13. Horiuchi T, Takahashi M, Li Q-H, Wang S, Sakai S (2010) Lowered operation voltage in Pt/$SBi_2Ta_2O_9$/HfO_2/Si ferroelectric-gate field-effect transistors by oxynitriding Si. Semicond Sci Technol 25:055005
14. Misirlioglu IB, Vasiliev AL, Aindow M, Alpay SP, Ramesh R (2004) Threading dislocation generation in epitaxial (Ba, Sr) TiO_3 films grown on (001) $LaAlO_3$ by pulsed laser deposition. Appl Phys Lett 84:1742–1744
15. Sharma A, Ban ZG, Alpay SP, Mantese JV (2004) Effect of operating temperature and film thickness on the pyroelectric response of ferroelectric materials. Appl Phys Lett 84:4959–4961
16. Okatan MB, Mantese JV, Alpay SP (2010) Effect of space charge on the polarization hysteresis characteristics of monolithic and compositionally graded ferroelectrics. Acta Mater 58:39–48
17. Okatan MB, Mantese J, Alpay S (2009) Polarization coupling in ferroelectric multilayers. Phys Rev B 79:174113
18. Eliseev EA, Morozovska AN (2009) General approach for the description of size effects in ferroelectric nanosystems. J Mater Sci 44:5149–5160. doi:10.1007/s10853-009-3473-0
19. Tenne DA, Soukiassian A, Xi XX, Taylor TR, Hansen PJ, Speck JS, York RA (2004) Effect of thermal strain on the ferroelectric phase transition in polycrystalline $Ba_{0.5}Sr_{0.5}TiO_3$ thin films studied by Raman spectroscopy. Appl Phys Lett 85:4124–4126
20. Haeni JH, Irvin P, Chang W, Uecker R, Reiche P, Li YL, Choudhury S, Tian W, Hawley ME, Craigo B, Tagantsev AK, Pan XQ, Streiffer SK, Chen LQ, Kirchoefer SW, Levy J, Schlom DG (2004) Room-temperature ferroelectricity in strained $SrTiO_3$. Nature 430:583–586
21. Misirlioglu IB, Vasiliev AL, Alpay SP, Aindow M, Ramesh R (2006) Defect microstructures in epitaxial $PbZr_{0.2}Ti_{0.8}O_3$ films grown on (001) $SrTiO_3$ by pulsed laser deposition. J Mater Sci 41:697–707. doi:10.1007/s10853-006-6488-9
22. Weiss CV, Okatan MB, Alpay SP, Cole MW, Ngo E, Toonen RC (2009) Compositionally graded ferroelectric multilayers for frequency agile tunable devices. J Mater Sci 44:5364–5374. doi:10.1007/s10853-009-3514-8
23. Han H, Lee K, Lee W, Alexe M, Hesse D, Baik S (2009) Fabrication of epitaxial nanostructured ferroelectrics and investigation of their domain structures. J Mater Sci 44:5167–5181. doi:10.1007/s10853-009-3528-2

24. Arredondo M, Saunders M, Petraru A, Kohlstedt H, Vrejoiu I, Alexe M, Browning ND, Munroe P, Nagarajan V (2009) Structural defects and local chemistry across ferroelectric-electrode interfaces in epitaxial heterostructures. J Mater Sci 44:5297–5306. doi:10.1007/s10853-009-3548-y
25. Lin Y, Chen CL (2009) Interface effects on highly epitaxial ferroelectric thin films. J Mater Sci 44:5274–5287. doi:10.1007/s10853-009-3664-8
26. Morioka H, Saito K, Yokoyama S, Oikawa T, Kurosawa T, Funakubo H (2009) Effect of film thickness on ferroelectric domain structure and properties of $Pb(Zr_{0.35}Ti_{0.65})O_3/SrRuO_3/SrTiO_3$ heterostructures. J Mater Sci 44:5318–5324. doi:10.1007/s10853-009-3606-5
27. Schlom DG, Chen LQ, Eom CB, Rabe KM, Streiffer SK, Triscone JM (2007) Strain tuning of ferroelectric thin films. Annu Rev Mater Res 37:589–626
28. Choi KJ, Biegalski M, Li YL, Sharan A, Schubert J, Uecker R, Reiche P, Chen YB, Pan XQ, Gopalan V, Chen LQ, Schlom DG, Eom CB (2004) Enhancement of ferroelectricity in strained $BaTiO_3$ thin films. Science 306:1005–1009
29. Sun F, Khassaf H, Alpay SP (2014) Strain engineering of piezoelectric properties of strontium titanate thin films. J Mater Sci 49:5978–5985. doi:10.1007/s10853-014-8316-y
30. Janolin PE (2009) Strain on ferroelectric thin films: example of $Pb(Zr_{1-x}Ti_x)O_3$. J Mater Sci 44:5025–5048. doi:10.1007/s10853-014-8316-y
31. Davis L, Rubin LG (1953) Some dielectric properties of barium-strontium titanate ceramics at 3000 megacycles. J Appl Phys 24:1194–1197
32. Haun MJ, Zhuang ZQ, Furman E, Jang SJ, Cross LE (1989) Thermodynamic theory of the lead zirconate-titanate solid solution system, part III : curie constant and sixth-order polarization interaction dielectric stiffness coefficients. Ferroelectrics 99:45–54
33. Soukiassian A, Tian W, Vaithyanathan V, Haeni JH, Chen LQ, Xi XX, Schlom DG, Tenne DA, Sun HP, Pan XQ, Choi KJ, Eom CB, Li YL, Jia QX, Constantion C, Feenstra RM, Bernhagen M, Reiche P, Uecker R (2008) Growth of nanoscale $BaTiO_3/SrTiO_3$ superlattices by molecular-beam epitaxy. J Mater Res 23:1417–1432
34. Specht E, Christen H-M, Norton D, Boatner L (1998) X-Ray diffraction measurement of the effect of layer thickness on the ferroelectric transition in epitaxial $KTaO_3/KNbO_3$ multilayers. Phys Rev Lett 80:4317–4320
35. Nakagawara O, Shimuta T, Makino T, Arai S, Tabata H, Kawai T (2002) Dependence of dielectric and ferroelectric behaviors on growth orientation in epitaxial $BaTiO_3/SrTiO_3$ superlattices. Vacuum 66:397–401
36. Kim L, Jung D, Kim J, Kim YS, Lee J (2003) Strain manipulation in $BaTiO_3/SrTiO_3$ artificial lattice toward high dielectric constant and its nonlinearity. Appl Phys Lett 82:2118–2120
37. Corbett MH, Bowman RM, Gregg JM, Foord DT (2001) Enhancement of dielectric constant and associated coupling of polarization behavior in thin film relaxor superlattices. Appl Phys Lett 79:815–817
38. Tabata H, Tanaka H, Kawai T (1994) Formation of artificial $BaTiO_3/SrTiO_3$ superlattices using pulsed laser deposition and their dielectric properties. Appl Phys Lett 65:1970–1972
39. Zubko P, Stucki N, Lichtensteiger C, Triscone J-M (2010) X-Ray diffraction studies of 180° ferroelectric domains in $PbTiO_3/SrTiO_3$ superlattices under an applied electric field. Phys Rev Lett 104:187601
40. Roytburd AL, Zhong S, Alpay SP (2005) Dielectric anomaly due to electrostatic coupling in ferroelectric-paraelectric bilayers and multilayers. Appl Phys Lett 87:092902
41. Okatan MB, Misirlioglu IB, Alpay SP (2010) Contribution of space charges to the polarization of ferroelectric superlattices and its effect on dielectric properties. Phys Rev B 82:094115
42. Tsurumi T, Harigai T, Tanaka D, Kakemoto H, Wada S (2004) Anomalous dielectric and optical properties in perovskite-type artificial superlattices. Sci Technol Adv Mater 5:425–429
43. Tsurumi T, Ichikawa T, Harigai T, Kakemoto H, Wada S (2002) Dielectric and optical properties of $BaTiO_3/SrTiO_3$ and $BaTiO_3/BaZrO_3$ superlattices. J Appl Phys 91:2284–2289
44. Neaton JB, Rabe KM (2003) Theory of polarization enhancement in epitaxial $BaTiO_3/SrTiO_3$ superlattices. Appl Phys Lett 82:1586–1588
45. Aguado-Puente P, García-Fernández P, Junquera J (2011) Interplay of couplings between antiferrodistortive, ferroelectric, and strain degrees of freedom in monodomain $PbTiO_3/SrTiO_3$ superlattices. Phys Rev Lett 107:217601
46. Zubko P, Jecklin N, Torres-Pardo A, Aguado-Puente P, Gloter A, Lichtensteiger C, Junquera J, Stephan O, Triscone J-M (2012) Electrostatic coupling and local structural distortions at interfaces in ferroelectric/paraelectric superlattices. Nano Lett 12:2846–2851
47. Misirlioglu IB, Kesim MT, Alpay SP (2014) Layer thickness and period as design parameters to tailor pyroelectric properties in ferroelectric superlattices. Appl Phys Lett 105:172905
48. Kumar A, Katiyar RS, Premnath RN, Rinaldi C, Scott JF (2009) Strain-induced artificial multiferroicity in $Pb(Zr_{0.53}Ti_{0.47})O_3/Pb(Fe_{0.66}W_{0.33})O_3$ layered nanostructure at ambient temperature. J Mater Sci 44:5113–5119. doi:10.1007/s10853-009-3503-y
49. Tsurumi T, Miyasou T, Ishibashi Y, Ohashi N (1998) Preparation and dielectric property of $BaTiO_3$–$SrTiO_3$ artificially modulated structures. Jpn J Appl Phys 37:5104–5107
50. Tsurumi T, Suzuki T, Yamane M, Daimon M (1994) Fabrication of barium titanate/strontium titanate artificial superlattice by atomic layer epitaxy. Jpn J Appl Phys 33:5192–5195
51. Tsurumi T, Harigai T, Tanaka D, Nam S-M, Kakemoto H, Wada S, Saito K (2004) Artificial ferroelectricity in perovskite superlattices. Appl Phys Lett 85:5016
52. Neaton JB, Rabe KM (2003) Theory of polarization enhancement in epitaxial $BaTiO_3/SrTiO_3$ superlattices. Appl Phys Lett 82:1586–1588
53. Stephenson GB, Elder KR (2006) Theory for equilibrium 180° stripe domains in $PbTiO_3$ films. J Appl Phys 100:051601
54. Specht ED, Christen H-M, Norton DP, Boatner LA (1998) X-Ray diffraction measurement of the effect of layer thickness on the ferroelectric transition in epitaxial $KTaO_3/KNbO_3$ multilayers. Phys Rev Lett 80:4317–4320
55. Jo JY, Chen P, Sichel RJ, Callori SJ, Sinsheimer J, Dufresne EM, Dawber M, Evans PG (2011) Nanosecond dynamics of ferroelectric/dielectric superlattices. Phys Rev Lett 107:055501
56. Levy P, Zhang S, Fert A (1990) Electrical conductivity of magnetic multilayered structures. Phys Rev Lett 65:1643–1646
57. Kesim MT, Cole MW, Zhang J, Misirlioglu IB, Alpay SP (2014) Tailoring dielectric properties of ferroelectric-dielectric multilayers. Appl Phys Lett 104:022901
58. Haun MJ, Furman E, McKinstry HA, Cross LE (1989) Thermodynamic theory of the lead zirconate-titanate solid solution system, part II: tricritical behavior. Ferroelectrics 99:27–44
59. Pertsev NA, Kukhar V, Kohlstedt H, Waser R (2003) Phase diagrams and physical properties of single-domain epitaxial $Pb(Zr_{1-x}Ti_x)O_3$ thin films. Phys Rev B 67:054107
60. Pertsev NA, Tagantsev AK, Setter N (2000) Phase transitions and strain-induced ferroelectricity in $SrTiO_3$ epitaxial thin films. Phys Rev B 61:R825–R829
61. Hlinka J, Márton P (2006) Phenomenological model of a 90° domain wall in $BaTiO_3$-type ferroelectrics. Phys Rev B 74:104104
62. Tagantsev AK (2008) Landau expansion for ferroelectrics: which variable to use? Ferroelectrics 375:19–27
63. Bratkovsky AM, Levanyuk AP (2009) Continuous theory of ferroelectric states in ultrathin films with real electrodes. J Comput Theor Nanos 6:465–489

64. Stephanovich VA, Luk'yanchuk IA, Karkut MG (2005) Domain-enhanced interlayer coupling in ferroelectric/paraelectric superlattices. Phys Rev Lett 94:047601
65. Christen H-M, Specht ED, Norton DP, Chisholm MF, Boatner LA (1998) Long-range ferroelectric interactions in $KTaO_3$/$KNbO_3$ superlattice structures. Appl Phys Lett 72:2535–2537
66. Levanyuk AP, Misirlioglu IB (2011) Phase transitions in ferroelectric-paraelectric superlattices. J Appl Phys 110:114109
67. Jain M, Majumder S, Guo R, Bhalla AS, Katiyar RS (2002) Synthesis and characterization of lead strontium titanate thin films by sol–gel technique. Mater Lett 56:692–697
68. Lee SW, Kwon OS, Han JH, Hwang CS (2008) Enhanced electrical properties of $SrTiO_3$ thin films grown by atomic layer deposition at high temperature for dynamic random access memory applications. Appl Phys Lett 92:222903
69. Misirlioglu IB, Kesim MT, Alpay SP (2014) Strong dependence of dielectric properties on electrical boundary conditions and interfaces in ferroelectric superlattices. Appl Phys Lett 104:022906
70. Sakai S, Takahashi M (2010) Recent progress of Ferroelectric-Gate Field-Effect transistors and applications to nonvolatile logic and FeNAND flash memory. Materials 3:4950–4964
71. Kandaswamy PK, Guillot F, Bellet-Amalric E, Monroy E, Nevou L, Tchernycheva M, Michon A, Julien FH, Baumann E, Giorgetta FR, Hofstetter D, Remmele T, Albrecht M, Birner S, Dang LS (2008) GaN/AlN short-period superlattices for intersubband optoelectronics: a systematic study of their epitaxial growth, design, and performance. J Appl Phys 104:093501
72. Dong L, Alpay SP (2012) Role of heteroepitaxial misfit strains on the band offsets of $Zn_{1-x}Be_xO$/ZnO quantum wells: a first-principles analysis. J Appl Phys 111:113714
73. Dong L, Mantese JV, Avrutin V, Ozgur U, Morkoc H, Alpay SP (2013) Strain induced variations in band offsets and built-in electric fields in InGaN/GaN multiple quantum wells. J Appl Phys 114:043715
74. Li YL, Hu SY, Tenne D, Soukiassian A, Schlom DG, Xi XX, Choi KJ, Eom CB, Saxena A, Lookman T, Jia QX, Chen LQ (2007) Prediction of ferroelectricity in $BaTiO_3$/$SrTiO_3$ superlattices with domains. Appl Phys Lett 91:112914
75. National Research Council (2008) Integrated computational materials engineering: a transformational discipline for improved competitiveness and national security. The National Academies Press, Washington, DC